

**Instrumental chapters**  
COMPASS thesis

Armando Brandonisio

June 20, 2016

# Contents

<b>1</b>	<b>Absorber characterization</b>	<b>3</b>
1.1	Absorber properties . . . . .	3
1.2	Experimental set-up . . . . .	5
1.3	Definition of the operative range . . . . .	10
1.3.1	Set-up parameters . . . . .	10
1.3.2	Expected efficiency . . . . .	10
1.4	Circuit calibration with X-ray sources . . . . .	11
1.4.1	Dark/Background noise . . . . .	14
1.5	Energy resolution measurement . . . . .	15
<b>2</b>	<b>Scatterer characterization</b>	<b>16</b>
2.1	Scatterer properties . . . . .	16
2.1.1	Intrinsic properties . . . . .	17
2.1.2	Coupling with SiPMs . . . . .	19
2.2	Study at low energy . . . . .	21
2.2.1	Set-up parameters . . . . .	21
2.2.2	Dark current comparison . . . . .	22
2.3	Study at high energy . . . . .	26
2.3.1	Set-up parameters . . . . .	26
2.3.2	Spectra analysis . . . . .	26
	<b>References</b>	<b>31</b>

# Chapter 1

## Absorber characterization

Characterization of scintillator rods is a fundamental starting point to understand possibilities and limits of the entire experiment.

Absorber bars are the external objects of polarimeter design, and they must be made of a high atomic number  $Z$  to maximize absorption of the radiation. A good light yield and emission velocity ( $\leq 1\mu s$ ) are recommended to optimize spectrum detection and coincidence measurements.

The agreement between absorber light emission spectrum and the photo-detection efficiency range of SiPM increases the collected charge of the readout process.

The measurements have been carried out by illuminating the scintillation rod with a X-ray beam.

SiPM and electronic chain parameters was varied measuring the relative position of the photo-peak in the spectrum produced by the scintillator.

### 1.1 Absorber properties

We investigated luminescence and scintillation properties of the  $Gd_3Al_2Ga_3O_{12}$  : Ce (GAGG) produced by *Furukawa* company.

The GAGG crystal has the highest light yield among oxide crystal at room temperature [1] and fast decay time for the detection of radioactivity and in nuclear and particle physics experiments.

A list of the most important parameters for GAGG is reported in Table 1.1.

Density [ $g/cm^3$ ]	Light yield [photon/MeV]	Decay time [ns]	Peak emission [nm]	Energy resolution [% @662 keV]	Hygroscopicity
6.63	57000	88 (91%) 258 (9%)	520	5.2	No

Table 1.1: Physical and scintillation properties of GAGG (data from [2])

Some fundamental features of this crystal are that it has no intrinsic radioactivity and it is a non-hygroscopic material. This allows a better usage for experimentation with low risk of contamination from ambient.

We know all GAGG properties (Tab 1.1) and cross section values with respect to energy. Results value in Fig 1.1.

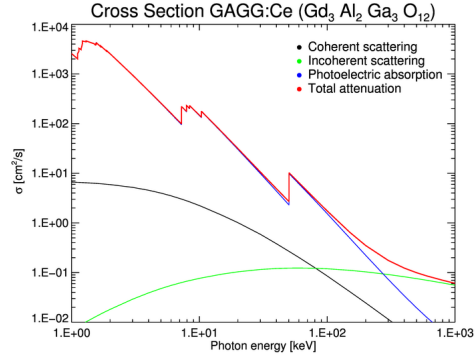


Figure 1.1: Mass attenuation coefficients for the GAGG crystal (Data from [3])

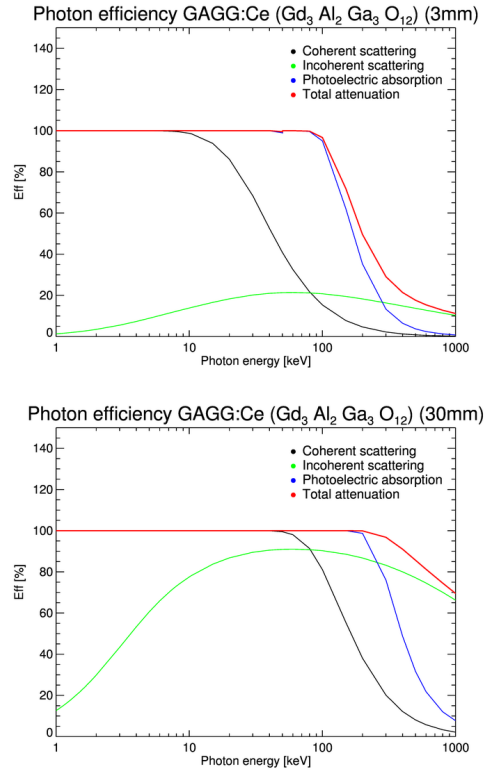


Figure 1.2: Total GAGG efficiency for a thickness of 3mm (left) and 30mm (right)

## 1.2 Experimental set-up

Laboratory measurements have been carried out using a single rod made of GAGG produced by *Furukawa* company.

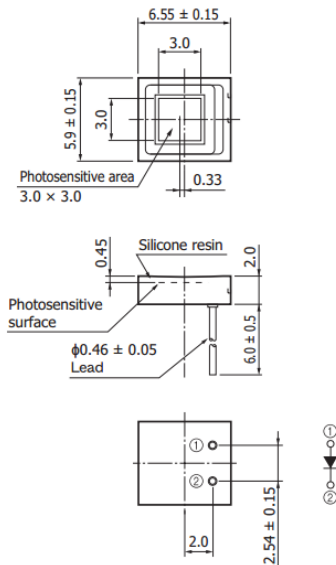
The rod has a square-base parallelepiped shape with a height of 30mm and a side of 3mm, thus their dimension results 2/3 lower to the one expected for the polarimeter bars ( $\sim 10\text{mm}$ ).

To minimize the loss of photons during scintillation, the bar was *wrapped* with Teflon tape Fig 1.3, that has a high light diffusion power.



Figure 1.3: Scintillation rod made of GAGG wrapped with teflon tape

The rod has been placed over a single SiPM, models LCT4/9 and LCT5/1 produced by the Hamamatsu company. Properties, CAD scheme and microscopic details of this SiPM are reported in Tab 1.2, Fig 1.4 and Fig 1.5 respectively.



### LCT4/9

Cell pitch	$75\mu\text{m}$
Device size	$3 \times 3\text{mm}^2$
Microcells	1600
Surface coating	Silicone resin
Fill-factor	73%
Breakdown	51.10 V

### LCT5/1

Cell pitch	$50\mu\text{m}$
Device size	$3 \times 3\text{mm}^2$
Microcells	3600
Surface coating	Silicone resin
Fill-factor	74%
Breakdown	52.5 V

Figure 1.4: CAD scheme for LCT4/9 and LCT5/1

Table 1.2: Main physical features of LCT/9 and LCT5/1

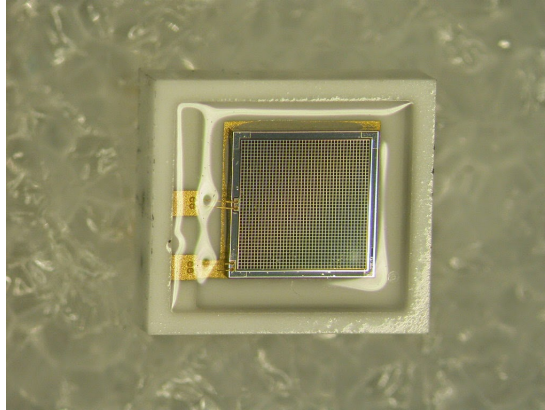


Figure 1.5: Image of LCT4/9 taken through a microscope.

This set of MPPCs produced by Hamamatsu, have an included proprietary circuit board with power supply for a direct hardware control from PC via USB connection (see Fig 1.6).

The C12332 is a simple evaluation starter kit for non-cooled MPPC. MPPC evaluation is possible by mounting an MPPC in the socket of the sensor circuit board. The power supply circuit board is equipped with the C11204-01, a high-accuracy, high-voltage power supply that provides the operating voltage from MPPC. It operates just by connecting to an external power supply ( $\pm 5V$ ). It is also equipped with a USB interface that can be used to set the operating voltage and temperature compensation coefficient from a PC running the supplied sample software.

We used the power supply circuit board with serial number C12332 with nominal gain of 21 for LCT4/9.

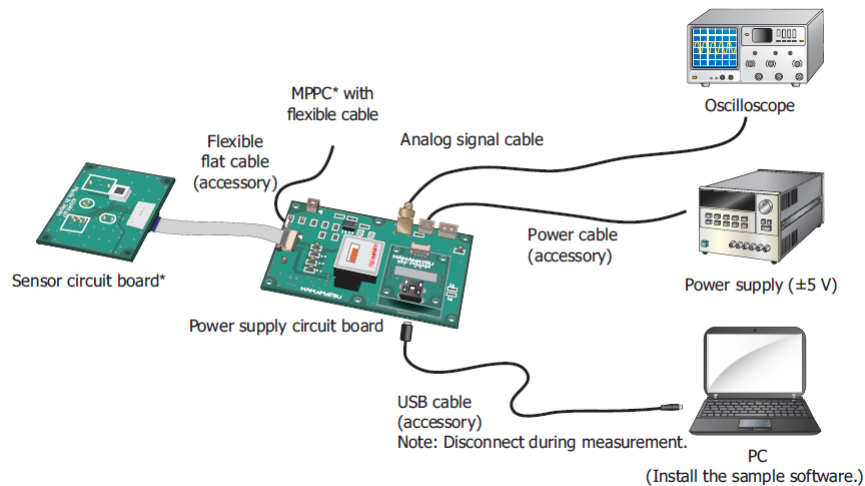


Figure 1.6: Connection example

Sensor circuit and power supply board have been both fixed on an aluminum support covered by black duct tape (Fig 1.7).

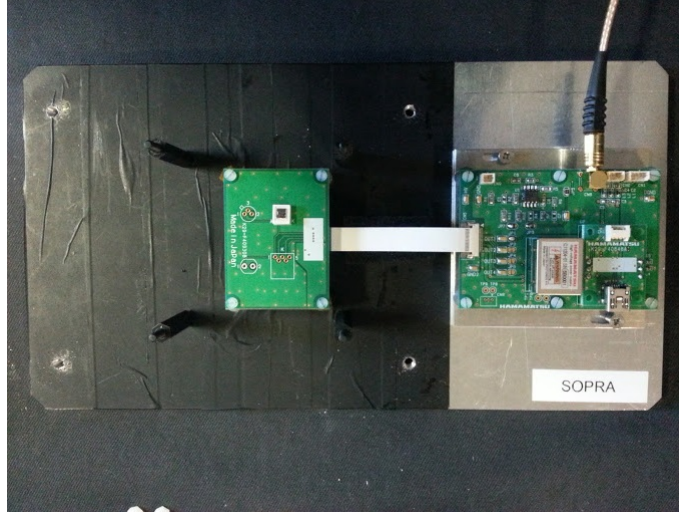


Figure 1.7: Circuit and sensor boards on support

The GAGG rod has been placed over a single SiPM. The extremity of the rod in contact with the SiPM window entrance has been covered with optical grease in order to improve the transmission of optical photons to the micro-cells.

A dedicated support has been projected and realized specifically for this experiment in order to hold the rod under study and to guarantee its contact with the SiPM.

The project drawing is reported in Fig 1.8 and the principal components legend below:

- (1) Aluminum support
- (2) secondary mobile support for power supply circuit board
- (4) dark box
- (6-7) support columns
- (8) support for rod-stops
- (9) rod stops
- (11) circular support for x-ray sources

The produced support inserted in the experimental set-up is shown in Fig 1.9.

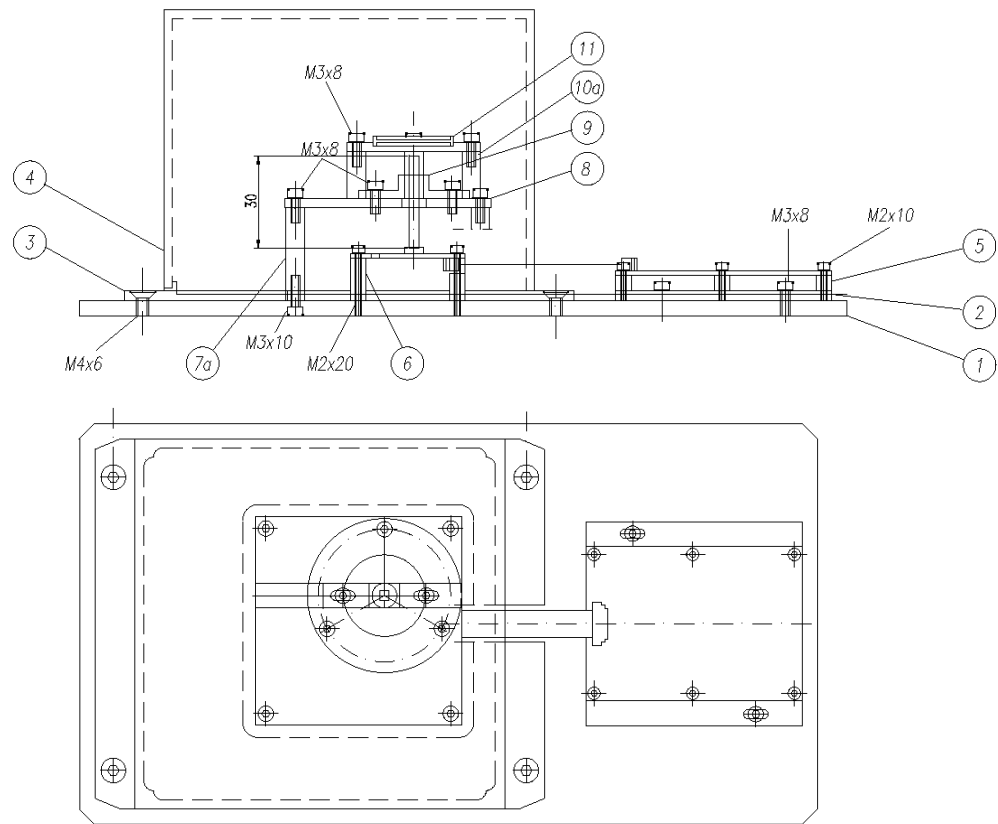


Figure 1.8: Front and side projection of entire setup.

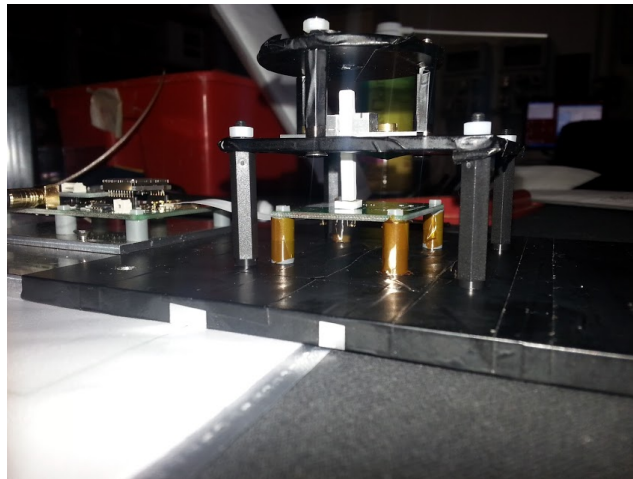


Figure 1.9: Built setup



Sources of  $^{241}\text{Am}$ ,  $^{109}\text{Cd}$ ,  $^{133}\text{Ba}$ ,  $^{55}\text{Fe}$ ,  $^{137}\text{Cs}$  have been used to illuminate the rod, placed at a distance of about  $5\text{mm}$  from the rod top, put on a circular aluminum support designed for the used radioactive sources (Fig. 1.9). The source, produced by *Eckert & Ziegler* company, has a diameter of  $3\text{mm}$  (Fig 1.10). It's flux has not been collimated.

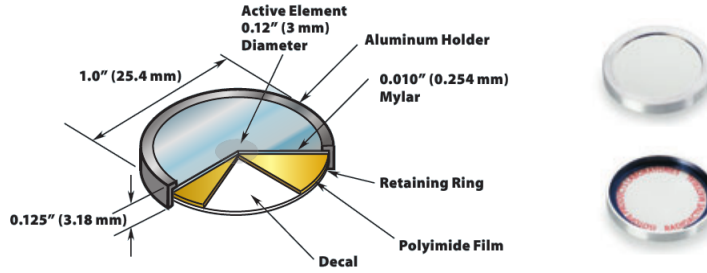


Figure 1.10: Type M disk used as x-rays source [4].

The alignment of the source along Z-direction has been carried out optically because the diameter of the beam spot was larger than the rod one, and therefore a rough alignment was sufficient.

The SiPM signal was read and processed by electronic chain whose diagram is reported in Fig 1.11. Power supply circuit board permitted to vary the operative voltage applied to the SiPM through USB connection and thus the SiPM internal gain.

The signal from SiPM was processed by a pre-amplifier welded on Hamamatsu circuit board and an amplifier ORTEC 450 *Research Amplifier*, and then digitized by a Multi-Channel Analyzer (MCA) Amptek 8000A, which splits signal into 1024 digital channels in a dynamic range of 0-5V or 0-10V.

The SiPM is very sensitive to visible light, therefore dark conditions are needed to perform the measurements. The dark conditions were assured by a *dark box* ((4) in Fig 1.8), a carton and a black cloth placed over the set-up.

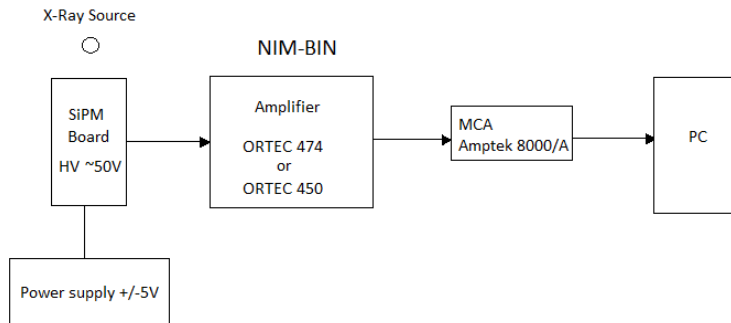


Figure 1.11: Sketch scheme of the electronic chain employed in the measurements to read and store SiPM signals

### 1.3 Definition of the operative range

#### 1.3.1 Set-up parameters

Some preliminary operations must be performed before starting the measurement process. In particular, the parameters of the electronic chain must be set to proper values, the digital channels of the MCA must be converted into charge values through a calibration and the experimental conditions must be analyzed.

The gains of the used SiPM and amplifier can be varied. It has been necessary to properly set these parameters in order to generate a signal within a range suitable to the MCA input dynamics.

During the adjusting process, the gains were changed until the whole signal from the SiPM has been included in the spectrum collected by the MCA. An intense light source was necessary to guarantee a high measurement rate in order to collect a suitable number of events in a short time and to dominate dark current.

We know that our GAGG rod has a light yield of  $\sim 60$  photons/keV [2] and the activity of the  $^{241}\text{Am}$  is  $\sim 10\mu\text{Ci}$ .

Here the instruments limitations:

- Hamamatsu datasheets says that we have a linearity of signal when we illuminate at the same time a number  $< 40\% - 50\%$  of MPPC pixels.
- MPPC signals are very fast ( $< 100\text{ns}$ ) and very frequents, but MCA accepts a minimum shaping time of  $250\text{ns}$  with a 'first peak detection'.

In order to prevent saturations or non-linearity in the final spectrum, we chose set-up parameters so that  $^{241}\text{Am}$  photo-peak @  $59.5\text{keV}$  was placed in the middle of MCA dynamic range.

Gain and integration time of ORTEC450 and *operative tension* ( $V_{op}$ ) of SiPMs have been changed to optimize quality of spectrum.

#### 1.3.2 Expected efficiency

To define an energy range of measurement system we needed to know maximum efficiency interval for scintillator rod, SiPMs and both. Detector efficiency, as function of energy, is defined by:

$$\epsilon(E) = T(E) \cdot A(E) \quad (1.1)$$

where  $T(E)$  and  $A(E)$  are respectively (1.2) transparency (1.3) and absorption with respect to energy radiation.

$$T(E) = e^{-\rho\delta\sigma(E)} \quad (1.2)$$

$$A(E) = 1 - e^{-\rho\delta\sigma(E)} \quad (1.3)$$

$\rho$  is the material density,  $\delta$  the thickness and  $\sigma(E)$  the cross section sums for coherent/incoherent Compton scattering and photoelectric effect as a function

of energy. Plotted results are showed in Fig 1.2.

From literature I have found the SiPMs quantum efficiency curve [5] and the GAGG light emission [6] to calculate the total efficiency of SiPM+GAGG system (Eq 1.4).

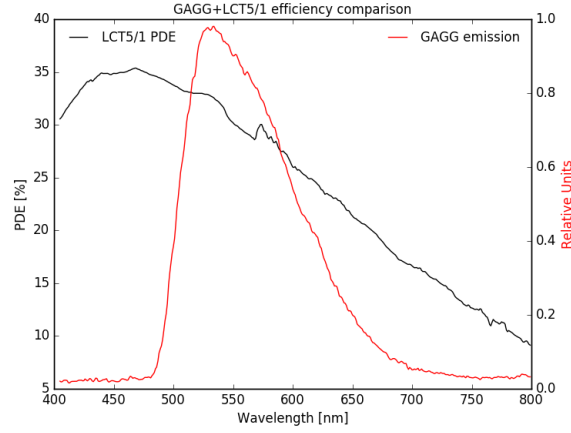


Figure 1.12: LCT5/1 QE and GAGG light emission

$$\epsilon_{tot} = \frac{\int_{\lambda} d\lambda \epsilon_{SiPM} \cdot \epsilon_{GAGG}}{\int_{\lambda} d\lambda \epsilon_{GAGG}} \quad (1.4)$$

Calculated efficiencies for LCT4/9 and LCT5/1 are listed in Tab 2.1.2.

SiPM	Tot. efficiency
LCT4/9 + GAGG	30.1%
LCT5/1 + GAGG	28.7%

Table 1.3: SiPM+GAGG efficiency

## 1.4 Circuit calibration with X-ray sources

I calibrated the electronic chain has been in order to convert the digital channels of the MCA output spectra in charge values.

Signals with similar amplitude, rise time and fall time of SiPM was produced by a pulse generator (BNC BL-2).

I measured the exact values of applied voltages through an oscilloscope connected to circuit. At the same time, the channel number of the peak produced by the signal in the MCA spectrum was stored and associated with the applied voltage.

This operation has been repeated for different  $V_{op}$  (Fig 1.13).

Furthermore an energy calibration was performed with radioactive sources described in section 1.1 (Fig 1.16).

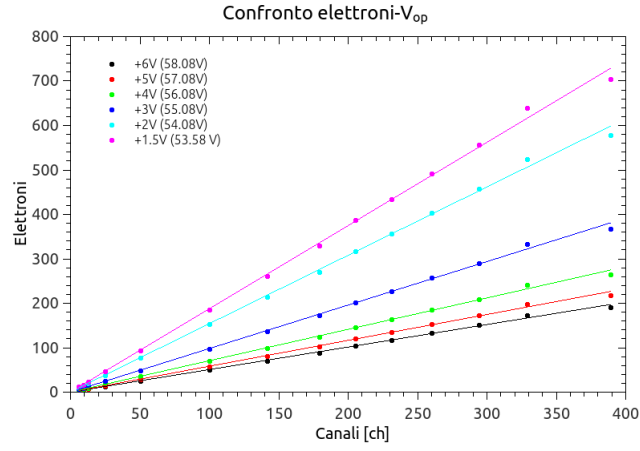


Figure 1.13: Linear calibration function used to convert the measured digital channels into charge values for LCT5/1.

I selected a gaussian model to fit sources photo-peaks. In order to improve fit, I studied a model that explain photopeak asymmetries for  $^{109}\text{Cd}$  and  $^{133}\text{Ba}$  (Fig 1.14).

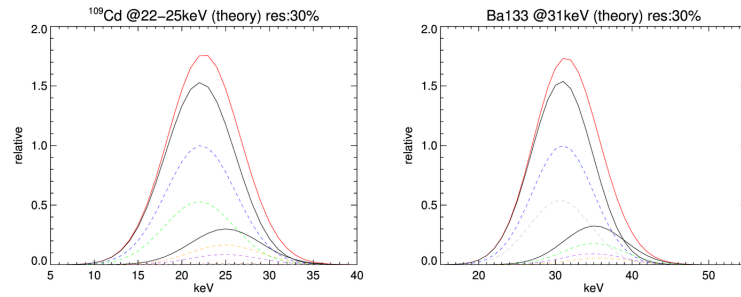


Figure 1.14: Theoretical model that assumes laboratory probability of each convoluted line for a resolution of 30%. Data from XCOM.

We also detected non-linearity for high energies values as expected (Fig 1.17).

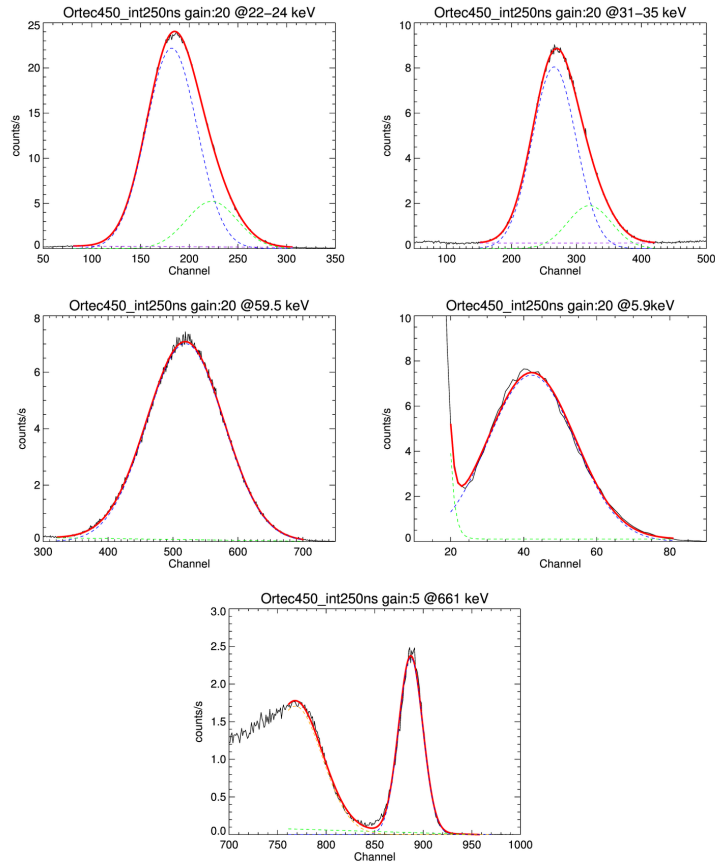


Figure 1.15: To left to right respectively:  $^{109}\text{Cd}$  @ 22keV,  $^{133}\text{Ba}$  @ 31keV,  $^{241}\text{Am}$  @ 59.5keV,  $^{55}\text{Fe}$  @ 5.9 keV,  $^{137}\text{Cs}$  @ 661 keV

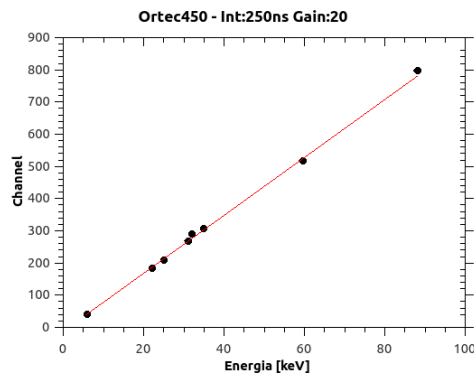


Figure 1.16: Linear energy calibration in the range of 0-90KeV for LCT4/9.

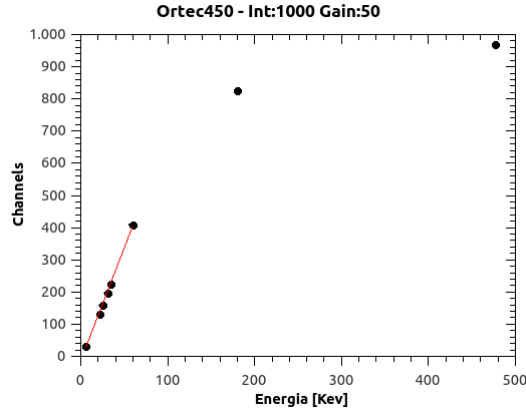


Figure 1.17: Non-linearity detection at high energies with LCT4/9.

#### 1.4.1 Dark/Background noise

Background noise spectra (Fig 1.18) are fundamental informations to select best configuration for acquiring data.

A study of *dark* counts has been performed to understand behavior of SiPM as  $V_{op}$  changes.

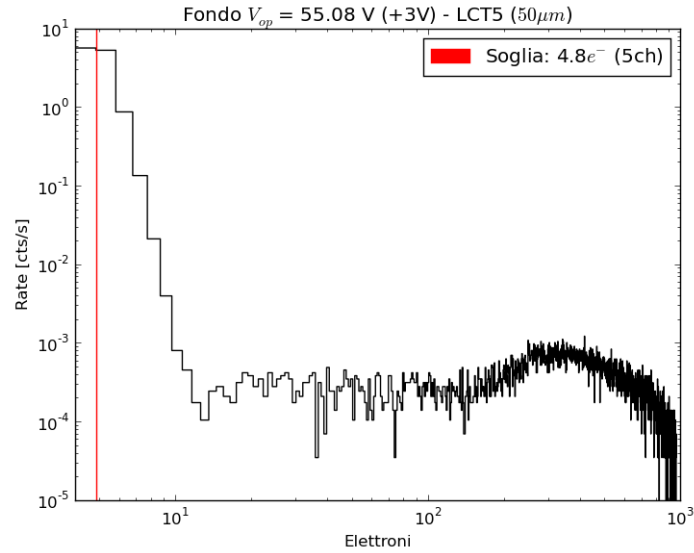


Figure 1.18: Background noise acquisition with LCT5/1 ( $V_{op} = +3V$ )+ GAGG.

Environmental noise is negligible with respect to sources rate. At low charge collection dark current dominates.

An exponential curve was chosen to fit dark noise (Fig 1.19).

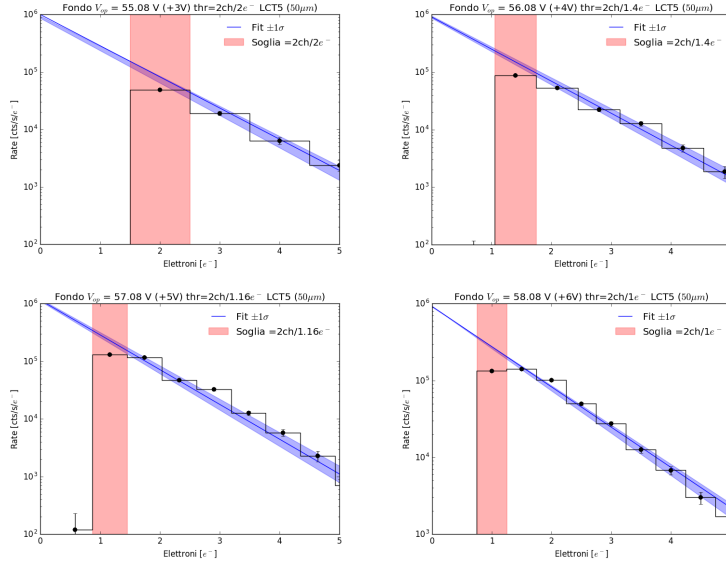


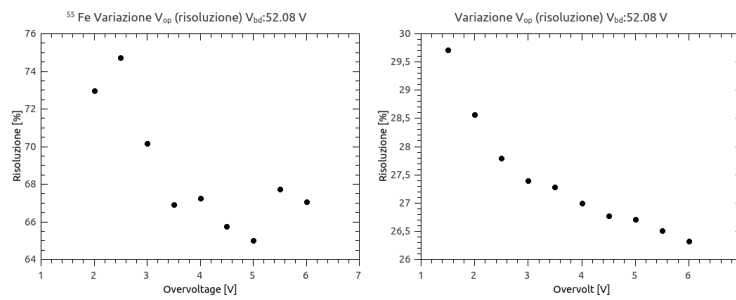
Figure 1.19: Dark rate study for LCT5/1+ GAGG

## 1.5 Energy resolution measurement

Fitted sources photopeaks of section 1.3 has been analyzed to extrapolate energy resolution as a function of  $V_{op}$ .

We note that dark rate increases with the increase of  $V_{op}$  but resolution seems to be better (decreases) with  $V_{op}$ .

Left plot of Fig 1.20 ( $^{55}\text{Fe}$  @ 5.9 keV), has an irregular distribution with respect to  $^{241}\text{Am}$  case, due to nearness of dark noise that affects error of photopeak position and width.

Figure 1.20: Resolution for  $^{55}\text{Fe}$  peak (left) and  $^{241}\text{Am}$  peak as function of  $V_{op}$ .

## Chapter 2

# Scatterer characterization

Scatterer rods are the inner components of Compton polarimeter design. They are made of plastic scintillator and wrapped with Teflon tape.

Plastic scintillators have a low atomic number  $Z$  which maximize the probability for the incident radiation to undergo Compton scattering.

These kind of scintillators have a light yield  $\sim 3$ -times lower than GAGG or high- $Z$  materials, for this reason I needed to change circuit board parameters to increase nominal gain.

The measurement have been carried out by illuminating the scintillation rod with a X-ray source.

The high-gain system allows to show the SiPM quantized spectrum, that has been analyzed with a ad-hoc software (discussed in the next chapter) to extract physical informations as resolution, calibration and collected charge.

### 2.1 Scatterer properties

I investigated luminescence and scintillation properties of plastic rods produced by *Eljen Technology*, listed in Tab 2.1.

Eljen Technology's plastic scintillators are based on a plastic matrix of polyvinyl-toluene ( $C_{27}H_{30}$ ) and fluors necessary to give each plastic scintillator its unique properties:

- **EJ-200:** combines the two important properties of long optical attenuation length and fast timing which make it particularly useful for time-of-flight systems using scintillators greater than one meter long. It is the detector of choice for many industrial applications, such as gauging and environmental protection, where high sensitivity and signal uniformity are critical operating requirements. [7]
- **EJ-204:** has the highest scintillation efficiency of any of Eljen's plastic scintillators, along with the combination of high speed and good attenuation length. It is particularly well suited for high-performance detector systems for nuclear and high-energy physics research. Its emission wavelength near 400 nm couples ideally with bialkali phototubes while still being long enough to be effectively used with UVT light guides. [7]



- **EJ-260:** is a green emitting plastic scintillator that has been formulated for use where longer wavelengths are advantageous for purposes of light piping. The green fluorescence is of short enough wavelength and the scintillation efficiency is high enough for successful use with conventional blue sensitive photomultiplier tubes. [8]

EJ-200 and EJ-204 have the properties of long optical attenuation length and fast timing with an emission spectrum well matched to common photomultipliers.

EJ-260 and green emitting plastic scintillators have been formulated for use where longer wavelengths are needed for efficient optical coupling to solid-state photosensors. Because of their longer emission wavelengths, they will exhibit somewhat greater radiation hardness than conventional blue plastic scintillators.

PROPERTIES	EJ-200	EJ-204	EJ-260
Light Output (% Anthracene)	64	68	60
Scintillation Efficiency (photons/1Mev $e^-$ )	10000	10400	9200
Wavelength of Maximum Emission [nm]	425	408	490
Light Attenuation Length [cm]	380	160	350
Rise Time [ns]	0.9	0.7	1.3
Decay Time [ns]	2.1	1.8	9.2
Pulse Width, FWHM [ns]	2.5	2.2	-
H Atoms per $cm^3$ ( $\cdot 10^{22}$ )	5.17	5.15	5.21
C Atoms per $cm^3$ ( $\cdot 10^{22}$ )	4.69	4.68	4.70
Electrons per $cm^3$ ( $\cdot 10^{23}$ )	3.33	3.33	3.35
Density [g/cm <sup>3</sup> ]	1.023	1.023	1.023
Polymer Base	Polyvinyltoluene		
Refractive Index	1.58		
Softening Point	75°C		
Vapor Pressure	Vacuum-compatible		
Coefficient of linear expansion	$7.8 \cdot 10^{-5}$ below 65°C		
Temperature Range	-20°C to 60°C		
Light Output vs. Temperature	At 60°C, L.O=95% of that at 25°C. No change from -60°C to 20°C		

Table 2.1: Scatterer rods properties from [7] [8].

### 2.1.1 Intrinsic properties

All Eljen plastic scintillator rods are made of Polyvinyltoluene ( $C_{27}H_{30}$ ), and small internal variations between EJ-200, EJ-204 and EJ-260 are negligible to study interaction with X-ray photons.

In Tab 2.1 are listed all basic features of used plastic scintillators, so I calculated mass attenuation coefficient with respect to photon energy between 1keV and 100 keV (Fig 2.1).

In the energy range of 1keV-10keV the photoelectric effect dominates. When energy photons is  $\sim 20$  keV, photoelectric effect and Compton effect are al-

most the same, and for energy between 20keV and 100keV Compton effect dominates.

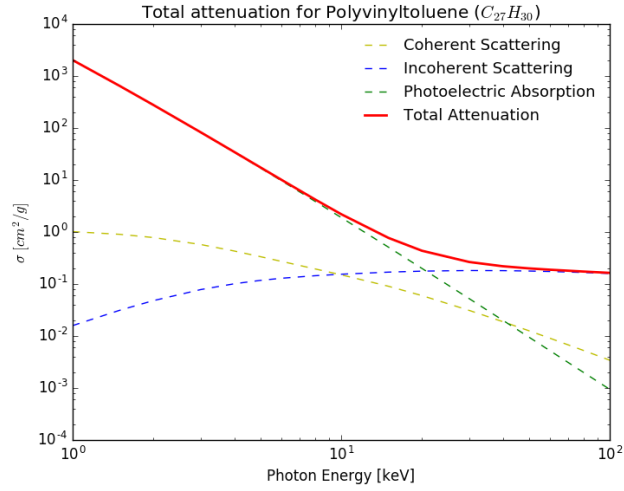


Figure 2.1: Mass attenuation coefficient for Eljen plastic scintillators. (Data from [3])

From equations ( 1.3) I calculated efficiency of total interactions for a 60mm thick rod (Fig 2.2).

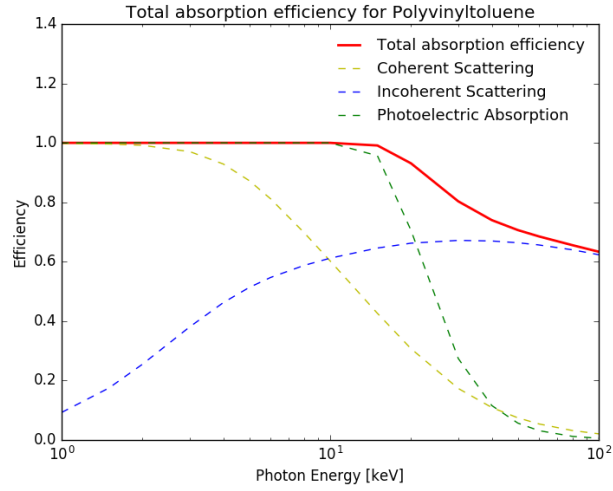


Figure 2.2: Total Polyvinyltoluene absorption efficiency for a thickness of 60mm

From Eljen datasheets [9] is reported that all plastic scintillators have the same response to atomic particles (Fig. 2.3).

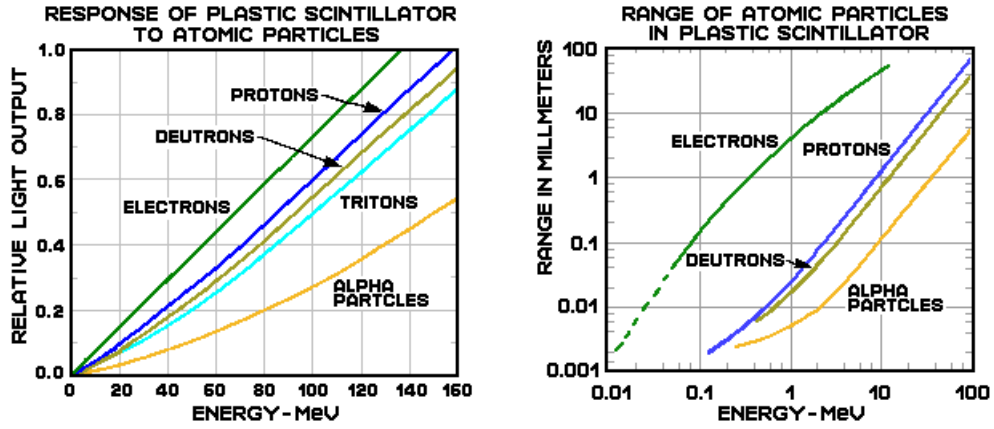


Figure 2.3: Response (left) and range of atomic particles in plastic scintillator (right). [9]

### 2.1.2 Coupling with SiPMs

The Eljen rods have been placed over a single SiPM. The extremity of the rod in contact with the SiPM window entrance has been covered with optical grease in order to improve the transmission of optical photons to the micro-cells.

Used scatterers have different emission spectra (Fig 2.4) and this makes different ways to optimize system efficiency when coupling with different SiPMs.

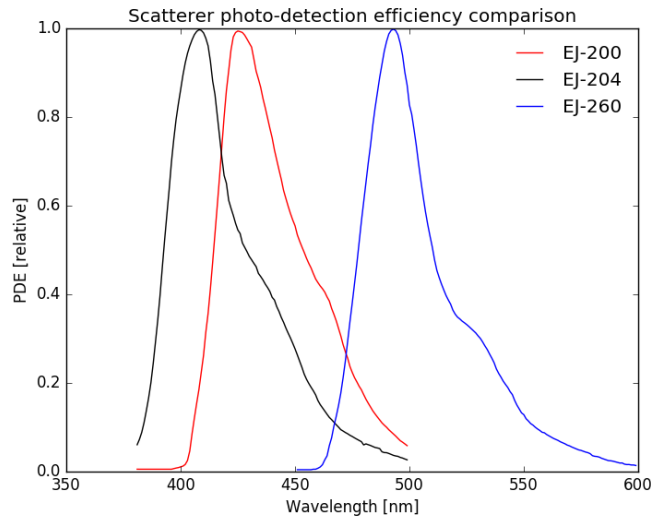


Figure 2.4: Emission spectrum of EJ-200 [9], EJ-204 [10], EJ-260 [11]

Used SiPM has been studied by Bonanno et al. [12] that measured their photon detection efficiency (PDE) (Discussed in [Capitolo sui SiPM](#)). I combined SiPMs PDE and scatterers emission spectra (Fig 2.5) to calculate total efficiency of a single rod case.

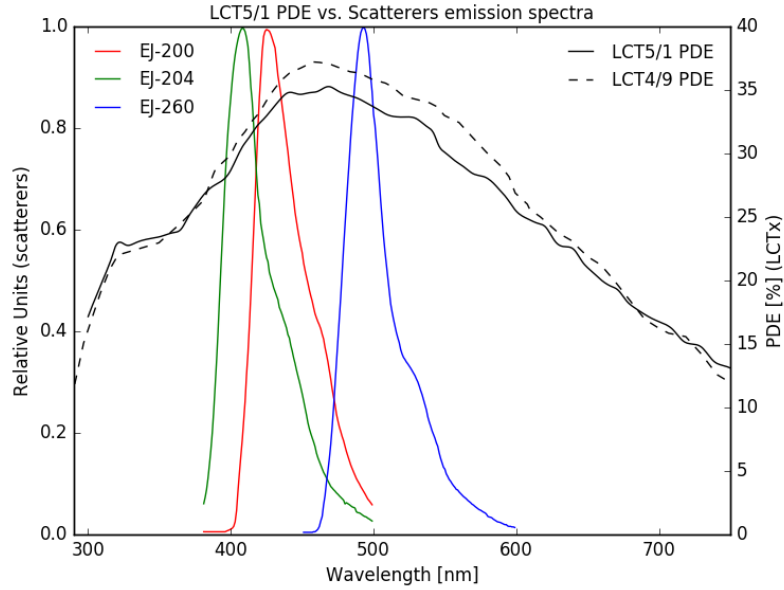


Figure 2.5: Comparison between SiPMs photon detection efficiency and scatterers emission spectra

In the ideal case, the overall system efficiency is:

$$\varepsilon_{tot} = \varepsilon_{SiPM} \cdot \varepsilon_{scatt} \cdot \varepsilon_{geom} \quad (2.1)$$

where  $\varepsilon_{SiPM}$  is the SiPM PDE,  $\varepsilon_{scatt}$  is the scintillator efficiency and  $\varepsilon_{geom}$  is the fraction of max light yield due to rod geometrical shape.

In realistic case I must add another term  $\varepsilon^*$  into equation 2.1 because there are additional factors that decrease overall efficiency, like light loss through the rod and imperfect coupling between scatterer and SiPM with optical grease, causing a further loss of light. So equation 1.3 becomes:

$$\varepsilon_{tot} = \varepsilon_{SiPM} \cdot \varepsilon_{scatt} \cdot \varepsilon_{geom} \cdot \varepsilon^* \quad (2.2)$$

All Eljen tested scintillators are made of the same polymer, so I can assume that  $\varepsilon_{geom} \cdot \varepsilon^*$  is the same for all scatterer rods ([probabilmente no, da rivedere](#)). For this reason I compared overall efficiencies normalized to  $\varepsilon_{geom} \cdot \varepsilon^*$  using 1.4. Results in Tab 2.1.2.

	LCT5/1	LCT4/9
Config.	Tot. Efficiency	Tot. Efficiency
EJ-200	33.7%	35.2%
EJ-204	31.5%	32.7%
EJ-260	32.7%	35.5%

Table 2.2: Overall efficiencies for SiPMs + scatterers system normalized to  $\varepsilon_{geom} \cdot \varepsilon^*$ .

## 2.2 Study at low energy

The first step of scatterer characterization is to choose SiPM with lower dark rate and better single photon resolution.

I tested and compared three types of SiPMs as power circuit board overvoltage varies.

### 2.2.1 Set-up parameters

Eljen plastic scintillators have a light yield  $\sim 3$ -times lower than GAGG, as discussed at the beginning of chapter. Therefore I needed to use a circuit board with increased nominal gain to 100. Used power supply circuit board was C12332 produced by Hamamatsu: the same tested for GAGG rod, but with an increased gain for preamplifier.

The experimental set-up was the same used for GAGG measurements (Fig 1.8) and the electronic chain is reported in Fig 2.6.

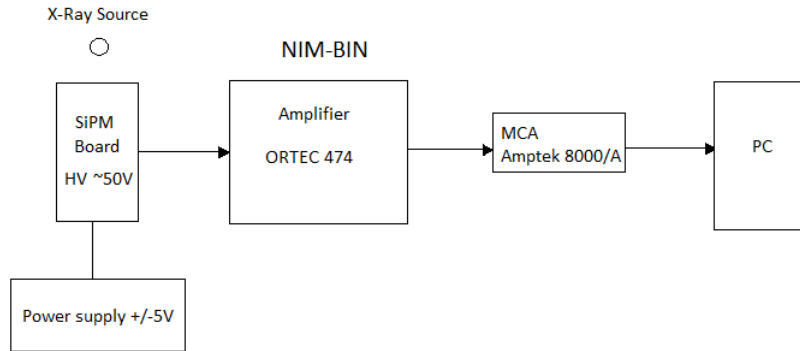


Figure 2.6: Sketch scheme of electronic chain employed in the measurements to read and store SiPMs+scatterers signals.

I chose the following parameters to perform measurements:

- Amplifier configuration (Ortec 474):
  - Coarse gain: 10
  - Fine gain: 2

- Integration time: 50 ns
- Differentiation: OUT
- MCA 8000A configuration:
  - dynamic range: 0-5 V
  - ADC channels: 4096

### 2.2.2 Dark current comparison

The aim of dark noise study is to choose the SiPM with better performances. The way is to find a well defined single photon spectrum with lowest counting rate at the same set-up conditions.

I studied dark current of LCT5/1 ( $50\mu m$ ), LCT4/9 ( $75\mu m$ ) and LCT4/20 ( $100\mu m$ ). LCT5 SiPMs, as discussed in ([capitolo sipm](#)), are new generation photomultipliers compared to LCT4 sensors, with sensitive reduction of afterpulses and crosstalk effects.

I measured and compared SiPMs spectra changing nominal overvoltage parameter.

I first studied considered SiPMs at nominal voltage (+3V) (Fig 2.7).

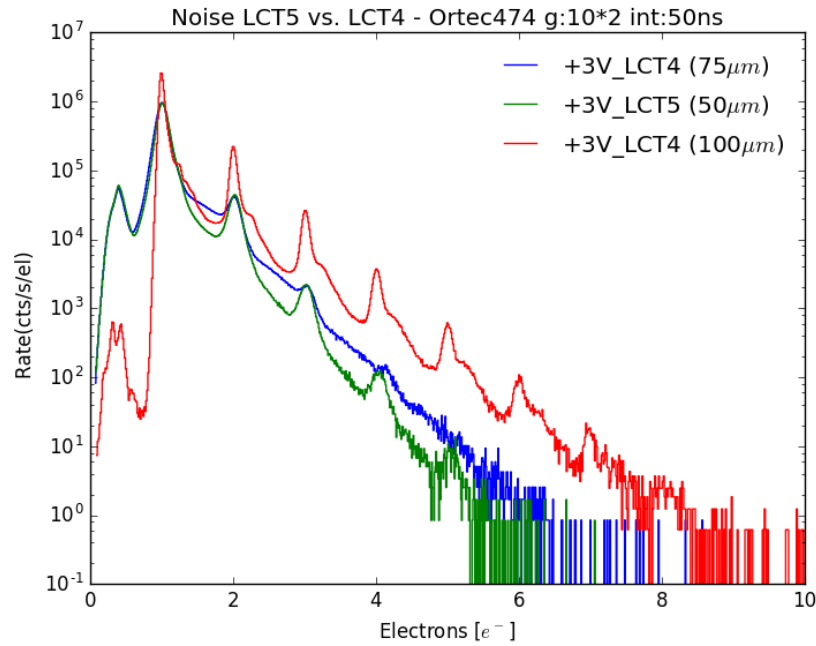


Figure 2.7: Dark rate comparison at nominal overvoltage for LCT5/1, LCT4/9 and LCT4/20.

LCT5/1 and LCT4/9 have a comparable single photon rate, but the first one has a better resolution that allows to distinguish all single photon spectra.

LCT4/20 has a good single photon resolution but higher counting rate compared to other SiPMs. Furthermore this sensor achieves an higher collected charge value ( $\sim 9e^-$ ) compared to others photomultipliers ( $\sim 6e^-$ ) and this affects signal to noise ratio.

I performed other measurements to varying of overvoltage between +2V and +5V:

- LCT5/1:

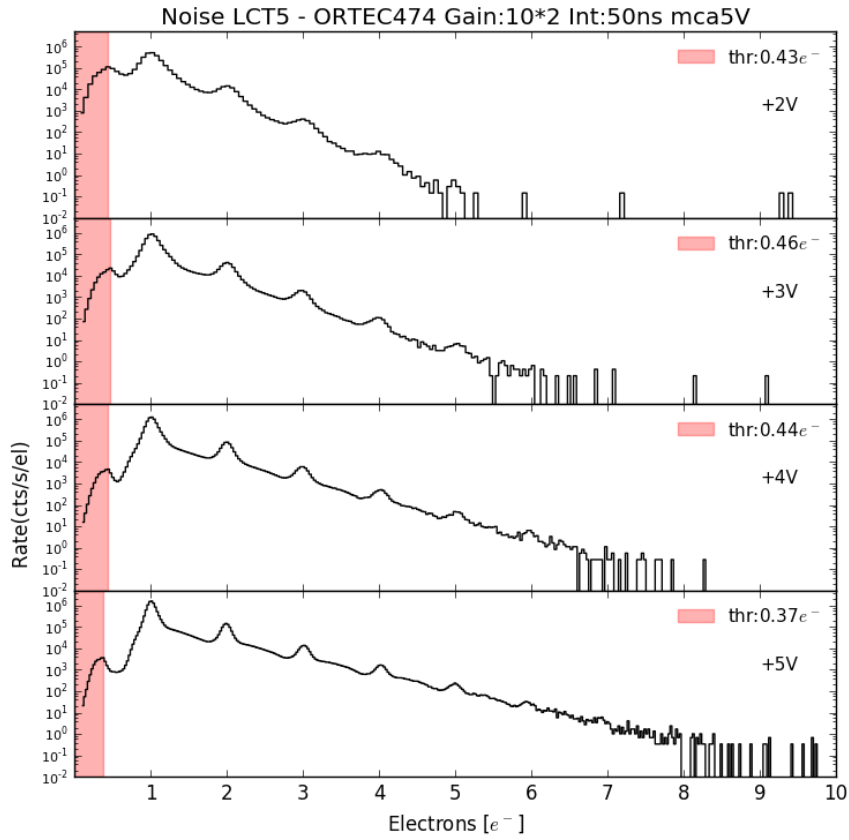


Figure 2.8: Dark rate comparison changing overvoltage for LCT5/1.

I integrated the same charge range for all overvoltage values to study noise total counts (Fig 2.9). Results are showed in Fig 2.10.

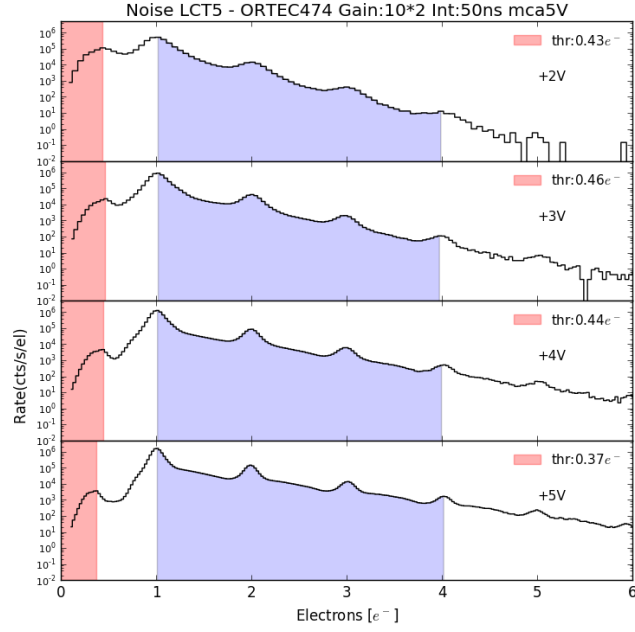


Figure 2.9: Noise integration between 1-4 PE for LCT5/1.

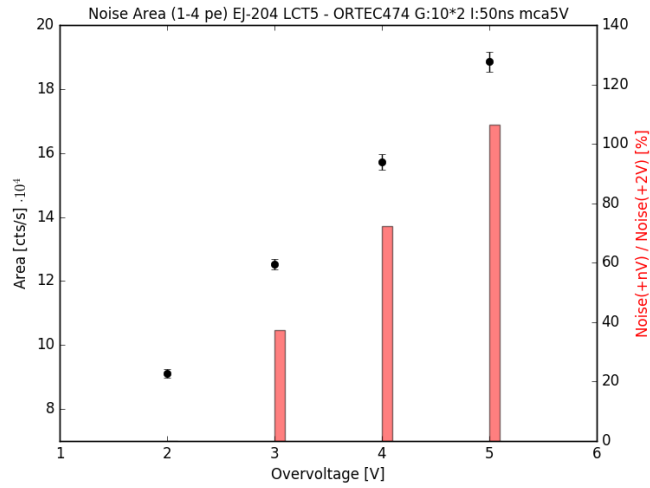


Figure 2.10: Integration results between 1-4 PE for LCT5/1.

The result is that increasing of overvoltage affects noise total rate of  $\sim 2$  times between +2V and +5V values (Fig 2.10).



- LCT4/9:

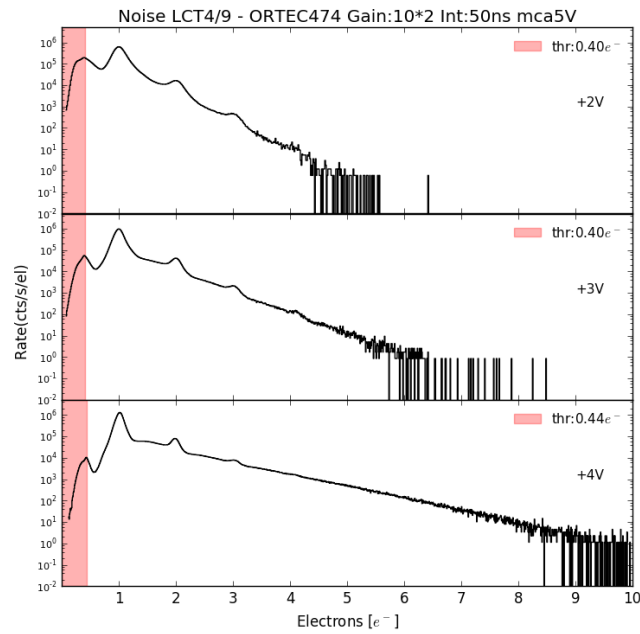


Figure 2.11: Dark rate comparison changing overvoltage for LCT4/9.

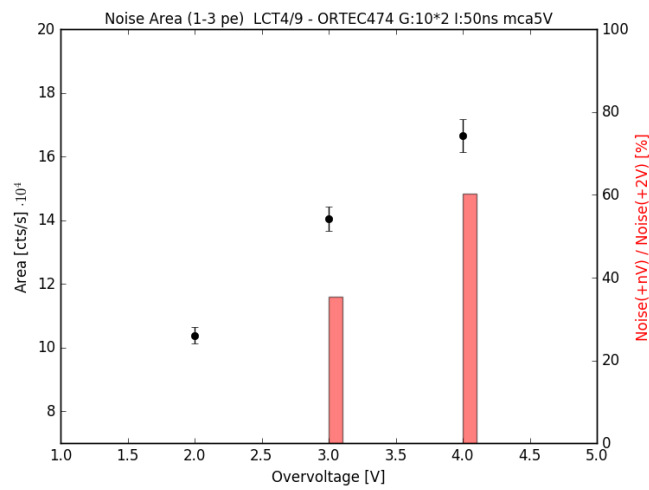


Figure 2.12: Integration results between 1-4 PE for LCT4/9.

Finally I chose LCT5/1 SiPM as best sensor for high energy measurements.

## 2.3 Study at high energy

After choosing SiPM with best performances, I coupled sensor with scintillators to perform measurements with X-ray source.

$^{109}\text{Cd}$  source has been used to illuminate the rods. It's activity was  $\sim 5.8\mu\text{Ci}(215\text{kBq})$  while acquiring data.

Used scintillators rods are EJ-200, EJ-204 and EJ-260, with a size of  $3\times 3\times 60\text{mm}$ . The aim of scatterers characterization is to achieve the highest charge collection with best resolution of source photo-peak changing overvoltage value.

### 2.3.1 Set-up parameters

The experimental set-up was the same described in Par 2.2.1, with one exception: coarse gain was 4 instead of 10.

In order to prevent saturation or non-linearity in the final spectrum, I chose this set-up parameters so  $^{109}\text{Cd}$  photo peak @ 22 keV was placed in the  $\sim 3/4$  of MCA dynamic range while overvoltage is +6V.

### 2.3.2 Spectra analysis

All spectra analysis was performed with an ad hoc python script (discussed in ...) written to accelerate and automate physical results.

An example of acquired spectrum with photo-peak is showed in fig 2.13.

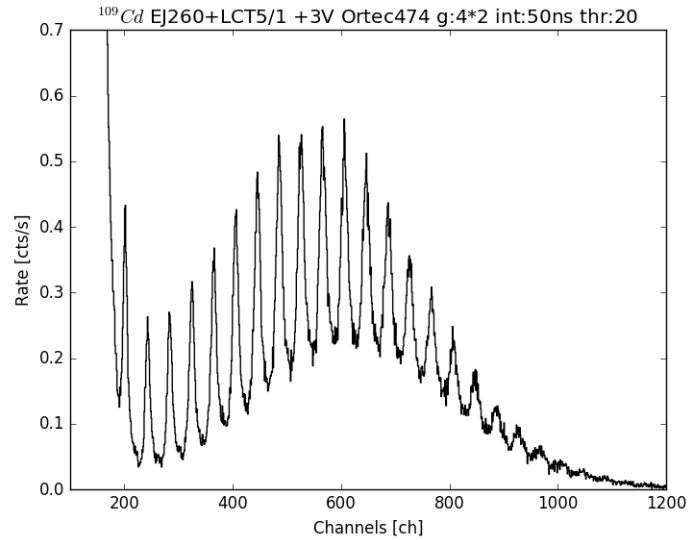


Figure 2.13: Acquired spectrum of  $^{109}\text{Cd}$  @ 22keV with EJ-260+ LCT5/1 (+3V).

As discussed in (cap sipm), SiPMs spectra at high gain are composed of multiple gaussian peaks for single photo-electron (PE) value that are distributed according to Poisson probability.

Physical properties of photo-peak need to be extracted integrating the whole spectrum with a multi-gaussian fit (Fig 2.14 and 2.15).

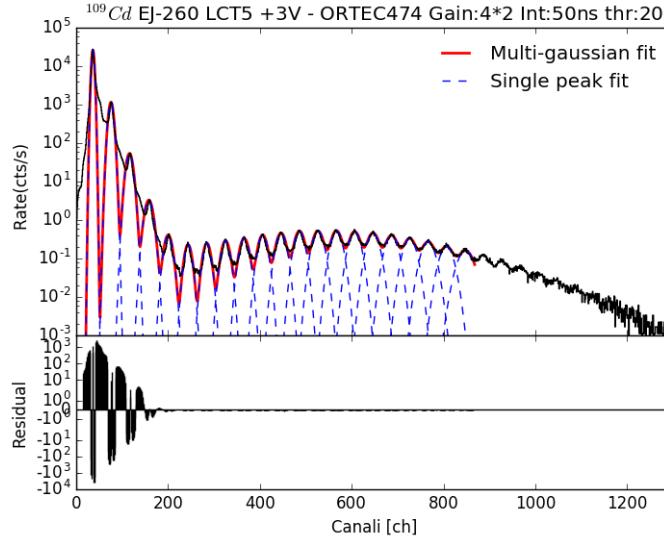


Figure 2.14: Integration of acquired spectrum of  $^{109}\text{Cd}$  @ 22keV with EJ-260+ LCT5/1 (+3V). The y-scale is Logarithmic to show the 4 orders of magnitude difference rate between dark noise and photo-peak.

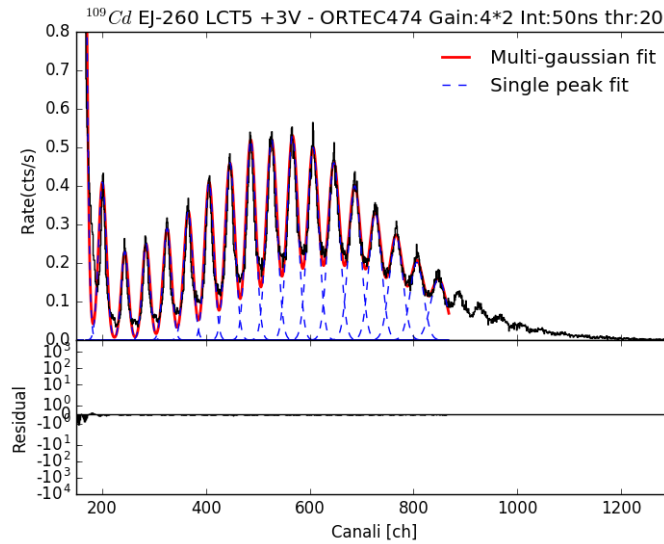


Figure 2.15: Integration of acquired spectrum of  $^{109}\text{Cd}$  @ 22keV with EJ-260+ LCT5/1 (+3V). (Linear scale)

With fit parameters I was able to study all main SiPM characteristics and photo-peak information, i.e. scatterer differences.

Linearity is well defined because of high number of single photon detection with a good resolution ( $\sim 10\%$ ), for this reason I calibrated ADC channels as function of photo-electrons number (Eq 2.3).

$$channel = A \cdot e^- + B \quad (2.3)$$

A calibration example is showed in Fig 2.16.

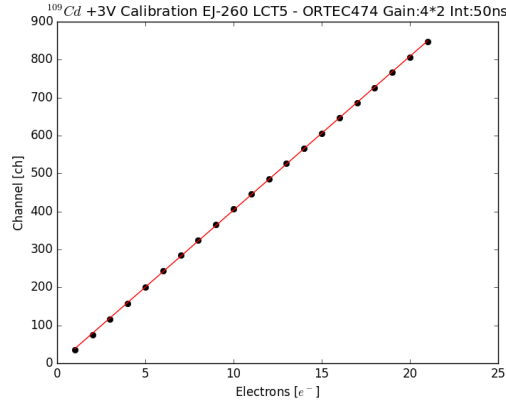


Figure 2.16: Calibration of integrated spectrum. [ $^{109}\text{Cd}$  @ 22keV with EJ-260+ LCT5/1 (+3V)].

I expected that difference between calibrated position of photon-electron peaks was  $\sim 1e^-$ . I considered this assumption as a further test for linearity (Fig 2.17).

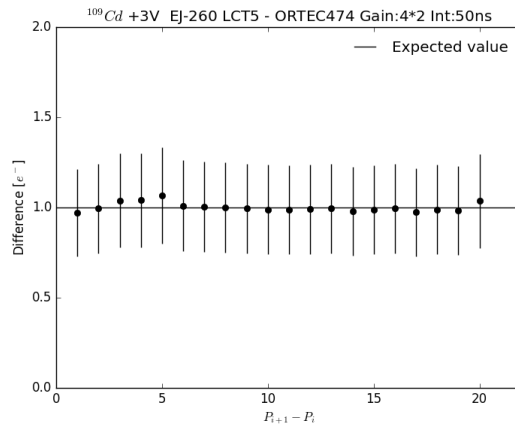


Figure 2.17: Differences between calibrated position of PE peaks. [ $^{109}\text{Cd}$  @ 22keV with EJ-260+ LCT5/1 (+3V)].

I obtained source photo-peak information integrating the area of single PE peaks. Fitting integrated points reveals information about position (collected charge), width (resolution) and rate. (Fig 2.18).

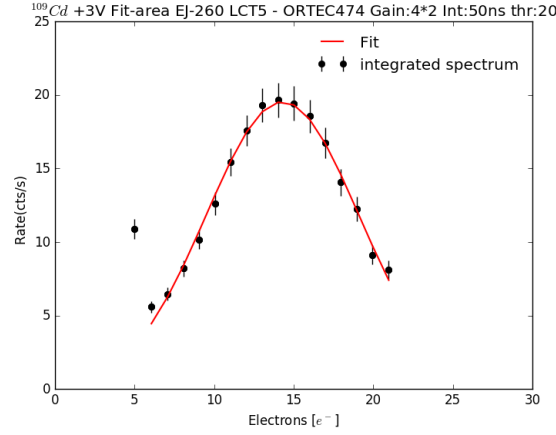


Figure 2.18: Integrated photo-peak area. [ $^{109}\text{Cd}$  @ 22keV with EJ-260+ LCT5/1 (+3V)].

SiPM spectrum has Poissonian distribution (discussed in ..), and therefore I expected a constant value for  $FWHM/\sqrt{N}$ , where FWHM is the width of single PE peaks and N is the number of considered PE. Result example in Fig 2.19.

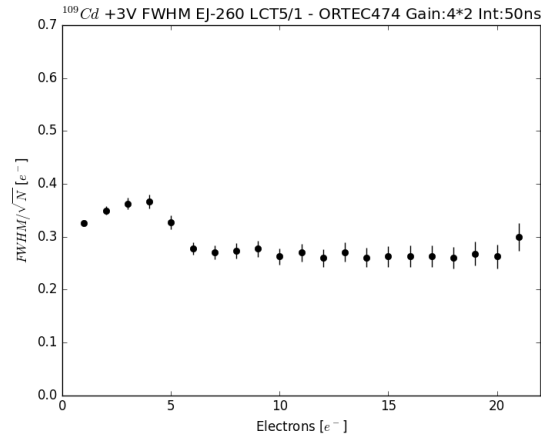


Figure 2.19:  $FWHM/\sqrt{N}$ . [ $^{109}\text{Cd}$  @ 22keV with EJ-260+ LCT5/1 (+3V)].

First PE width values (1 to 5  $e^-$ ) are quite inconsistent compared to high energy peaks, because of high rate that causes peak distortion and consequently a difficulty to fit curves increasing errors.

Other distortions are introduced by increasing the overvoltage value, that makes totally asymmetric peaks (Fig 2.20).

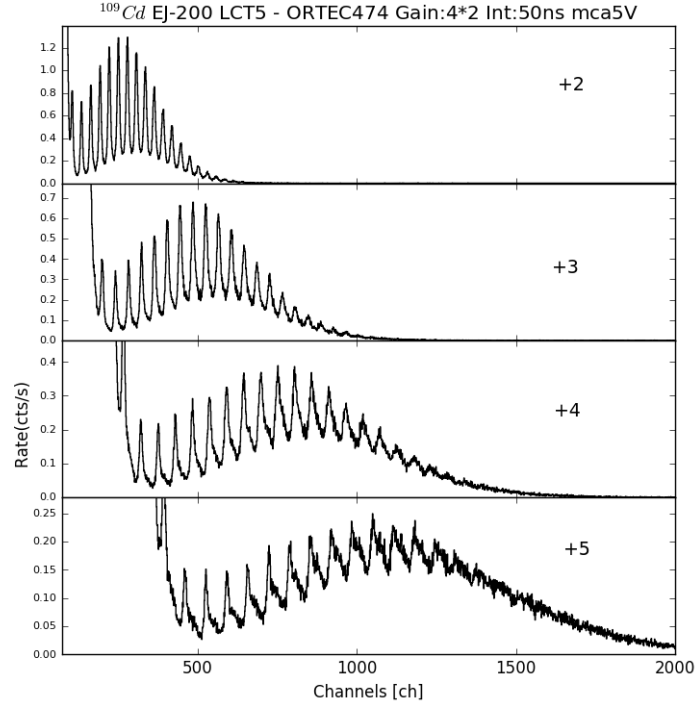


Figure 2.20: Acquired spectrum of  $^{109}\text{Cd}$  @ 22keV with EJ-260+ LCT5/1 (+3V) while varying overvoltage.

In this case used software does not converge while fitting, therefore I calculated position and photo-peak area by numerical integration. This way is logically more inaccurate than analytical study, because I can't elaborate a model that explains right distortions due to SiPM impurities and pile-up events.

I analyzed EJ-200, EJ-204 and EJ-260 spectra using explained methodology. Calibration results are listed in Tab (..) and fit results in Tab (..).

## TABELLE

# Bibliography

- [1] Hye-Lim Kim et al. Journal of Ceramic Processing Research. Vol. 16, No. 1, pp. 124-128, 2015
- [2] *Ce:GAGG Scintillator Crystal*, datasheet from Furukawa website (<http://www.furukawa-denshi.co.jp/cgi-bin/pdfdata/20140428162950.pdf>)
- [3] XCOM: Photon Cross Sections Database <http://www.nist.gov/pml/data/xcom/>
- [4] Section Gamma and X-Ray Standards. [http://www.ezag.com/fileadmin/ezag/user-uploads/isotopes/isotopes/Isotrak/isotrak-pdf/Product\\_literature/EZIPL/Gamma\\_Standards\\_All\\_Types.pdf](http://www.ezag.com/fileadmin/ezag/user-uploads/isotopes/isotopes/Isotrak/isotrak-pdf/Product_literature/EZIPL/Gamma_Standards_All_Types.pdf)
- [5] Bonanno et al. doi:10.1016/j.nima.2015.10.064
- [6] Seferis et al. doi:10.1007/978-3-319-00846-2-113, 2013
- [7] General purpose plastic scintillator, EJ-200, EJ-204, EJ-208, EJ-212. [http://www.eljentechnology.com/images/products/data\\_sheets/EJ-200\\_EJ-204\\_EJ-208\\_EJ-212.pdf](http://www.eljentechnology.com/images/products/data_sheets/EJ-200_EJ-204_EJ-208_EJ-212.pdf)
- [8] Green emitting plastic scintillator, EJ-260, EJ-262. [http://www.eljentechnology.com/images/products/data\\_sheets/EJ-260\\_EJ-262.pdf](http://www.eljentechnology.com/images/products/data_sheets/EJ-260_EJ-262.pdf)
- [9] EJ-200 plastic scintillator. <http://www.ggg-tech.co.jp/maker/eljen/ej-200.html>
- [10] EJ-204 plastic scintillator. <http://www.ggg-tech.co.jp/maker/eljen/ej-200.html>
- [11] EJ-260 plastic scintillator. <http://www.ggg-tech.co.jp/maker/eljen/ej-260.htm4>
- [12] Bonanno et al., NIM A, 806, 383, 2016